International Journal of Applied Earth Observations and Geoinformation 112 (2022) 102892

Contents lists available at ScienceDirect

International Journal of Applied Earth Observations and Geoinformation

journal homepage: www.elsevier.com/locate/jag

# Drainage congestion due to road network on the Kosi alluvial Fan, Himalayan Foreland

Abhilash Singh, Mood Niranjan Naik, Kumar Gaurav *

*Department of Earth and Environmental Sciences, Indian Institute of Science Education and Research Bhopal, Madhya Pradesh 462066, India*

ARTICLE INFO

*Keywords:*
Soil moisture
Road network
Deep learning
Drainage congestion

ABSTRACT

We use surface soil moisture content as a proxy to assess the effect of drainage congestion due to structural barriers on the alluvial Fan of the Kosi River on the Himalayan Foreland. We used Sentinel-1 satellite images to evaluate the spatial distribution of soil moisture in the proximity of structural barriers (*i.e.,* road network). We applied modified Dubois and a fully connected feed-forward artificial neural network (FC-FF-ANN) models to estimate soil moisture. We observed that the FC-FF-ANN predicts soil moisture more accurately (R = 0.85, RMSE = 0.05 $m^3/m^3$, and bias = 0) as compared to the modified Dubois model. Therefore, we have used the soil moisture from the FC-FF-ANN model for further analysis.

We identified the road network that traverses on the Kosi Fan horizontally, vertically, and with inclination. We create a buffer of 1 km along either side of the road. Within this, we assessed the spatial distribution of soil moisture. We observed a high concentration of soil moisture near the structural barrier, and decreases gradually as we move farther in either direction across the orientation of the road. The impact of structural barriers on the spatial distribution of soil moisture is prominent in a range between 300 to 750 m within the road buffer. This study is a step towards assessing the effect of structural interventions on drainage congestion and flood inundation.

## 1. Introduction

Engineering interventions (*i.e.,* rail-road network, embankments) on alluvial plain can act as barriers. They obstruct drainage networks that can sometimes lead to localised impoundment during the rainfall. If such a situation persists for a longer duration, it can lead to a permanent waterlogging in the regions. A condition that degrades the land and eventually affects the plant growth due to poor soil aeration, decrease in the soil pH, and nitrogen deficiency by the biological breakdown of the nitrate in the soil (Steffens et al., 2005; Ciancio et al., 2021).

Several studies have been conducted to identify waterlogged patches from remote sensing images (Pandey et al., 2012; Kaushik et al., 2019; den Besten et al., 2021; Jalayer et al., 2014; Singh and Sinha, 2022). A prior knowledge of the severity of drainage congestions can help to mitigate their impact. To perceive this, researchers have used the site inherent information (*i.e.,* soil hydraulics and topography) to assess drainage congestion (Hatton et al., 2002). For example, regions with sandy clay and silty loam soils are prone to drainage congestion due to their low infiltration capacity (McFarlane, 1985). Further, the regions with shallow groundwater levels are more prone to waterlogging (Chandio et al., 2012; Sinha et al., 2018). Alluvial Fan of the Kosi River in the Himalayan Foreland is well known for frequent flooding, severe waterlogging, and drainage congestion (Sinha et al., 2008; Sinha, 2014; Mishra and Sinha, 2020). Drainage congestion has not only affected agriculture productivity, but it has posed freshwater supply, shelter, sanitation, and other socioeconomic challenges. According to Sinha (2009), construction of embankments to control floods and other infrastructural development such as the road-rail network has resulted in severe drainage congestion on the Kosi Fan. Further, they have significantly altered the structural and functional connectivity of the channels (Sinha et al., 2013; Kumar et al., 2014). As a consequence, in recent years, the duration and area of flood inundation have increased on the Kosi Fan (Sinha et al., 2008). It is therefore utmost important to monitor drainage congestion due to the structural barriers.

The surface soil moisture content depends on the soil hydraulics and topography (Seibert et al., 2007; Florinsky, 2016; Yuan et al., 2021). It can be used as a proxy to assess the impact of drainage congestion. Generally, infiltration is less if the soil is saturated (high moisture); this

* Corresponding author.
*E-mail address:* kgaurav@iiserb.ac.in (K. Gaurav).

https://doi.org/10.1016/j.jag.2022.102892
Received 12 April 2022; Received in revised form 20 June 2022; Accepted 23 June 2022
Available online 1 July 2022

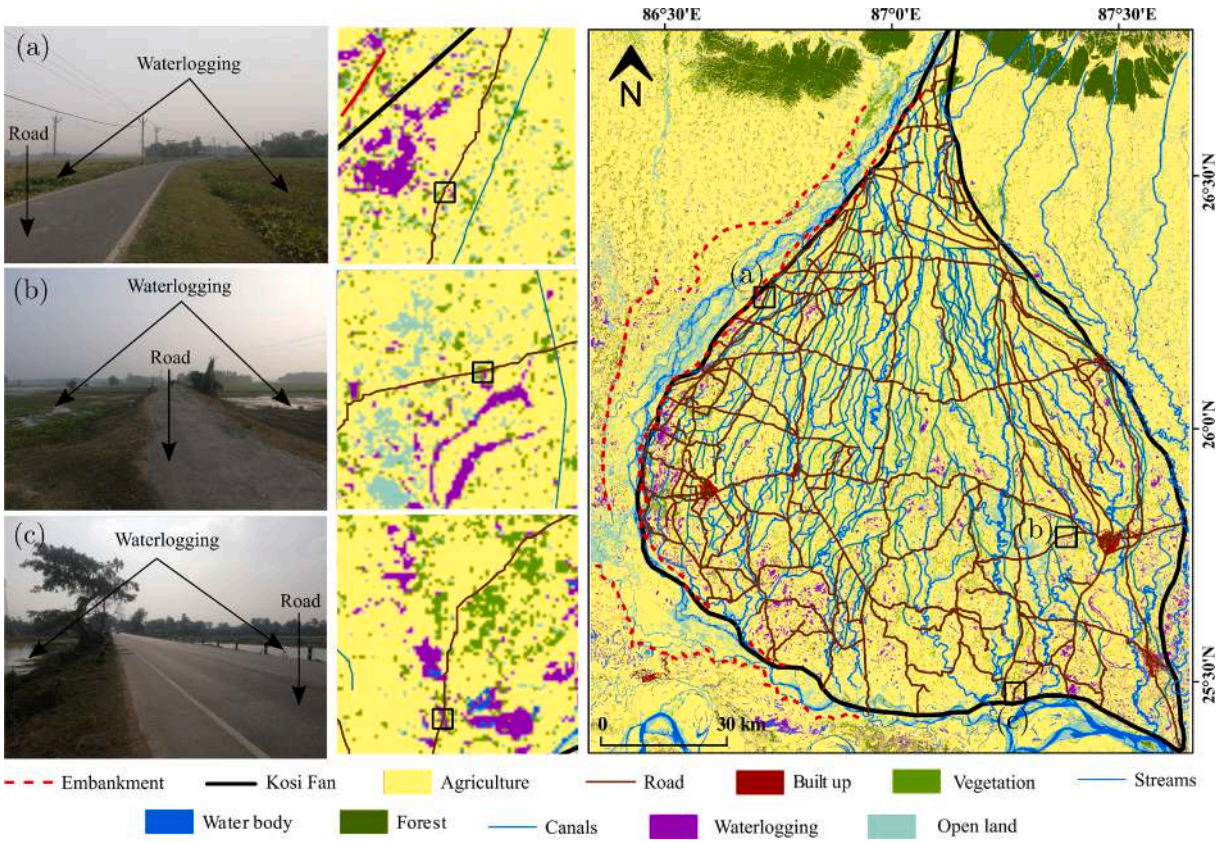


**Fig. 1.** Landuse/Landcover map of the study area (Source: NRSC). The conical boundary (in solid black) illustrates the extent of the Kosi Fan. Engineering structures such as, embankments (lines in dotted red), road (lines in solid dark red-brown), and canal (line in solid blue) are overlaid on the study area. Field photographs (a-c) on the left panel show the waterlogging in the proximity of road network.

**Table 1**
Description of the satellite data used in this study.

| Sentinel-1A/B | | | | |
|---|---|---|---|---|
| **Date** (mm-dd-yyyy) | **Polarisation** (Dual) | **Angle of Incidence** (°) | **Cell size** (m × m) | **Pass** |
| 12/11/2019 | (VV, and VH) | 38.6 | 10 × 10 | Descending |
| 12/15/2019 | -do- | 38.5 | -do- | Ascending |
| 12/17/2019 | -do- | 38.4 | -do- | Descending |
| 12/18/2019 | -do- | 38.5 | -do- | -do- |
| 12/20/2019 | -do- | 38.5 | -do- | Ascending |
| **Sentinel-2A/B** | | | | |
| **Date** (mm-dd-yyyy) | **Orbit number and direction** | **Bands** | **Wavelength** (nm) | **Spatial Resolution** |
| 12/09/2019 | 76, Descending | 4, 8 | 646–685, 774–907 | 10 m |
| **Shuttle Radar Topography Mission (SRTM)** | | | | |
| **Date** (mm-dd-yyyy) | **Grid spacing** | **Parameter** | **Co-ordinates** | **Spatial Resolution** |
| 09/23/2014 | 1 arc-second | Elevation | (25°–26° N, 86°–87° E) | 30 m |

eventually results in the storage of water on the surface for a longer duration. Such a condition can lead to a flood-like situation during the rainy season. Satellite remote sensing (microwave, optical) images have been used effectively to estimate surface soil moisture at regional and global scales by using various backscatter and data-driven machine learning models (Crow et al., 2017; Abowarda et al., 2021).

To the best of our knowledge, none of the existing literature utilised the soil moisture information to develop methodologies for assessing drainage congestion due to structural barriers. We propose a novel approach to identify the impact of drainage congestion along the road network. We use surface soil moisture as a proxy to measure the extent of drainage congestion in the proximity of structural barriers. We apply machine learning model to predict surface soil moisture from satellite (microwave and optical) images and in-situ measurements.

## 2. Study area

We carried this study on the Kosi alluvial Fan (Fig. 1). It is one of the largest alluvial Fan (≈ 150 km length and ≈ 115 km width) on the Himalayan Foreland (Wells and Dorr, 1987; Sinha, 2009; Sinha, 2014; Gaurav et al., 2015; Gaurav et al., 2017).

The Kosi Fan is composed of homogeneous quartz grains with a median size ranging from 300 $\mu$m (medium sand) to 100 $\mu$m (fine sand) in the proximal and distal part, respectively (Gaurav et al., 2015). The major portion of the Fan is agricultural land (84%), with sandy, sandy loam, loam, and silty loam as the dominant soil type. The remaining portions are wetlands/water bodies (9%) and built-up (7%) (NRSC, 2017). The Kosi Fan lies in the tropical humid climate zone, and it annually receives 1,484 mm of rainfall. The minimum (winter) and

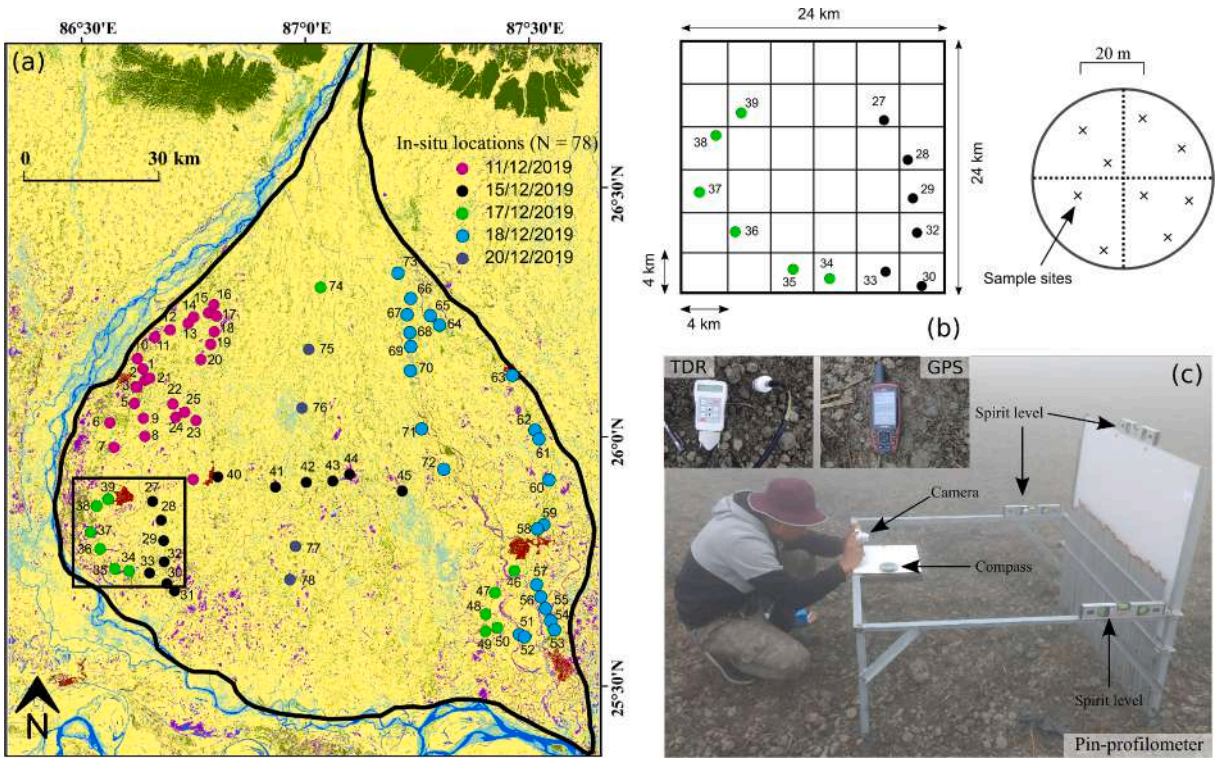


**Fig. 2.** (a) Landuse/landcover map of the Kosi Fan (Source: NRSC). Points in different colours represent the measurement made on different dates. Figures on the right panel, (b) illustrates the universal random grid sampling strategy adopted for the measurement of soil attributes (*i.e.,* moisture and surface roughness), (c) field photographs to show the different instruments used for the measurement of soil moisture (TDR), surface roughness (pin-profilometer), and location (GPS).

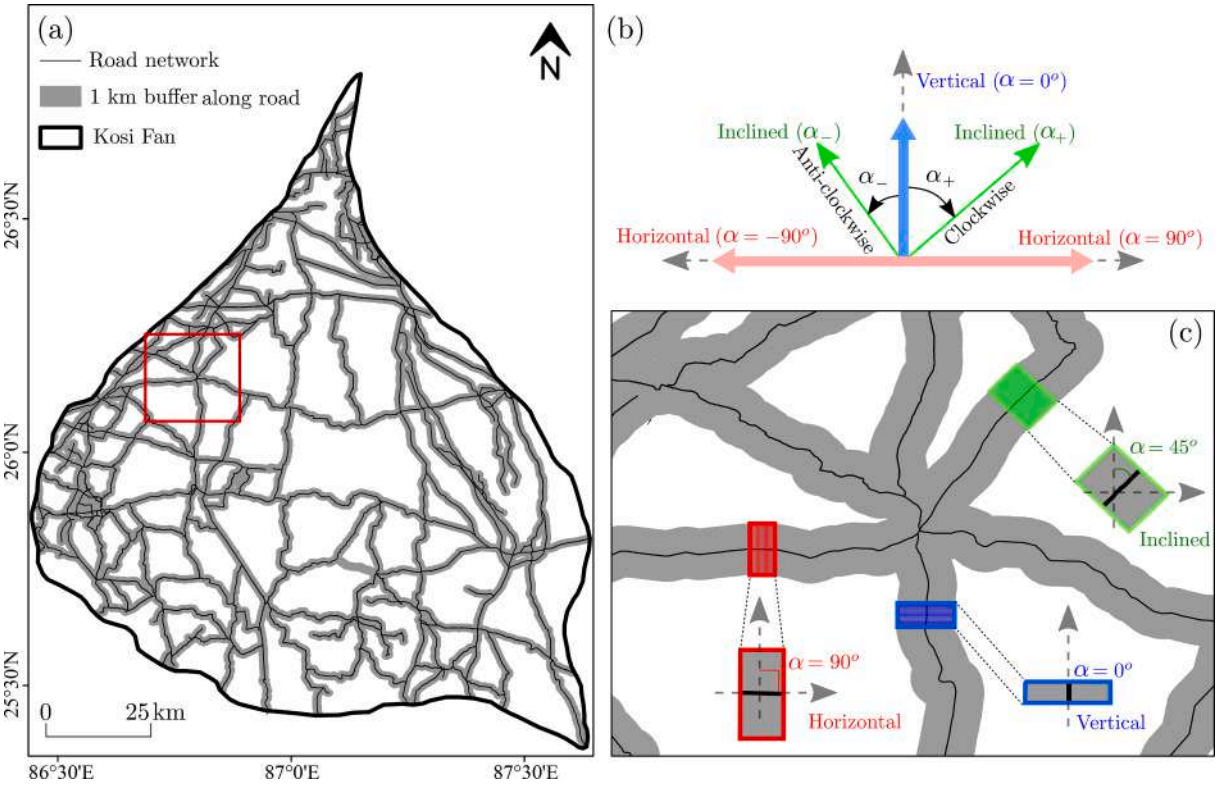


**Fig. 3.** (a) Road network (in black) with 1 km buffer (in shaded gray) on the Kosi megafan, (b) schematic illustrates the orientation (vertical, inclined, and horizontal) of road network, and (c) zoomed area (Fig. 3a box in red) illustrates the angle measurement along the road network.

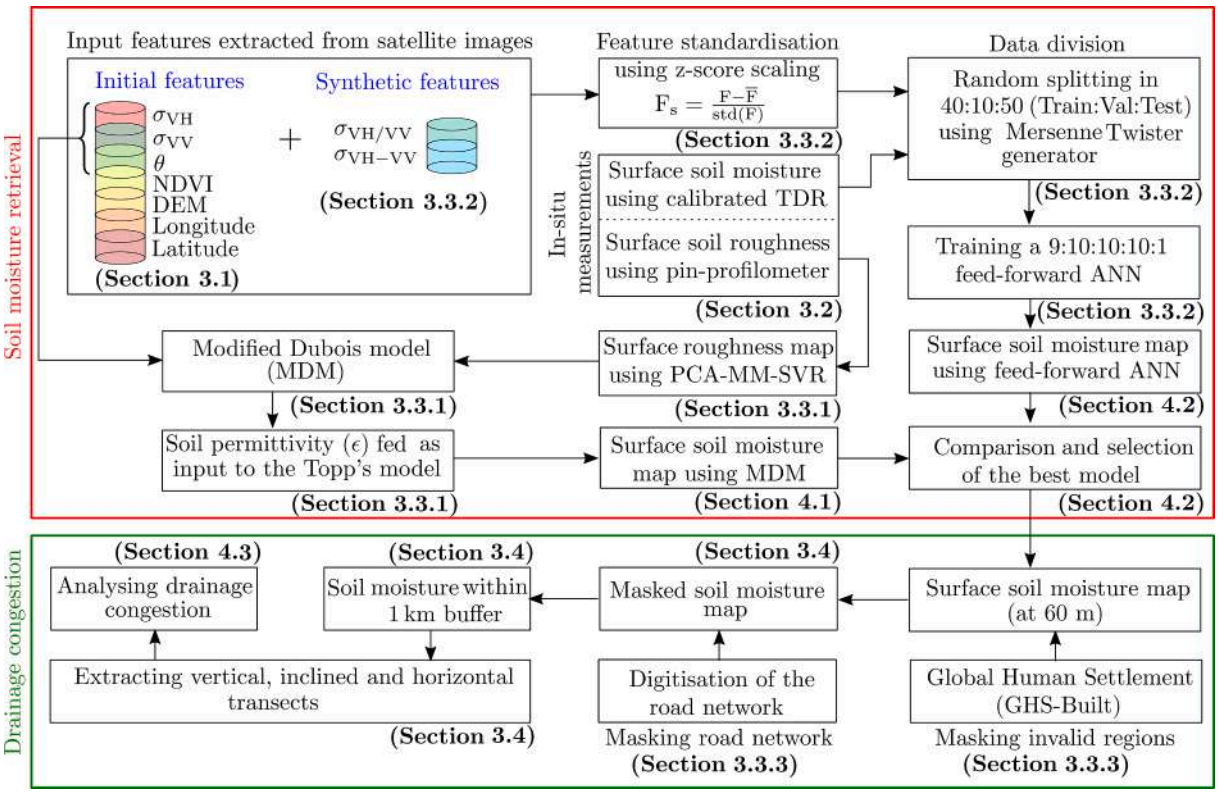


**Fig. 4.** Flow chart of the methodology. This study contains two parts, the first part (in red box) illustrates the detailed procedure opted to model soil moisture from Sentinel-1 images. Second part (in green box) shows the methodology used for the analysis of drainage congestion in the proximity of road network.

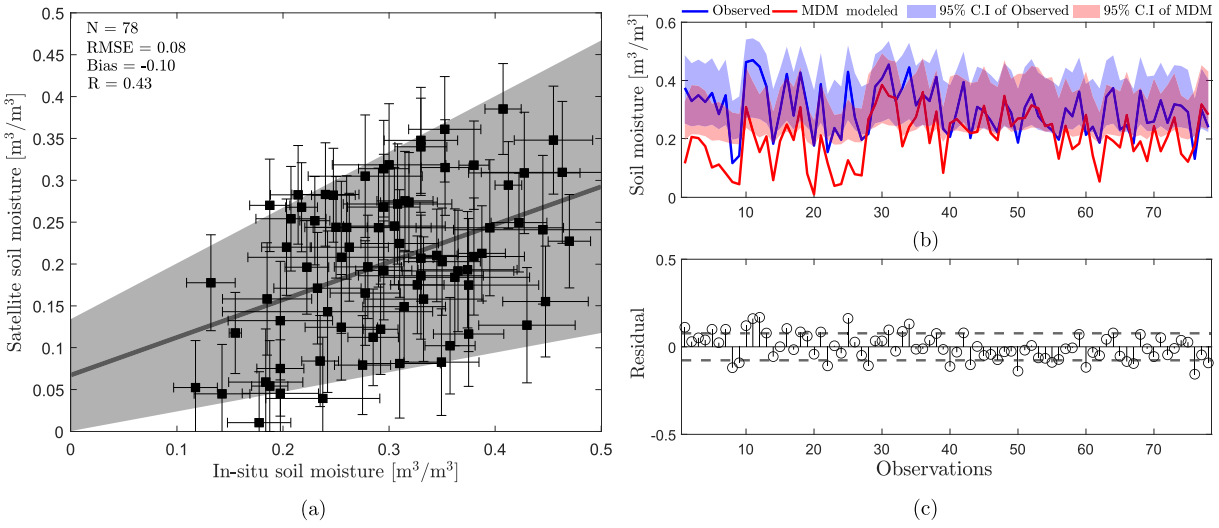


**Fig. 5.** (a) Satellite derived soil moisture (MDM) plotted as a function of in-situ data. Shaded region in gray represents the 95% confidence interval. Horizontal error bar is the standard deviation in the in-situ measurements, the vertical error bar is the model response to the input uncertainties, (b) represents time-series of observed and MDM-derived soil moisture with the 95% confidence level, and (c) represents the corresponding residual plot which is calculated by subtracting fitted values from the in-situ. The dashed lines represent the ±RMSE.

maximum (summer) average temperature range from 18°C to 32°C, respectively. The groundwater level is shallow and ranges from ≈ 1 to ≈ 8 m below ground level (bgl) throughout the year (http://cgwb.gov.in/).

In the past few decades, constructions of road-rail networks on the Kosi Fan has increased significantly (Kumar et al., 2014). In particular, this region observed a significant development of road-rail networks after the year 2010. On the Kosi Fan, majority of the roads traverse in the East - West direction, and most of the streams flows from North to South. As a consequence, they act as physical barriers to the streams, and there is a high chance of waterlogging in the proximity of these barriers. We have highlighted three such examples in Fig. 1 (a-c). We can observe the waterlogging along both sides of the road. To identify and monitor the potential regions for waterlogging in the study area, soil moisture can be used as a precursor.

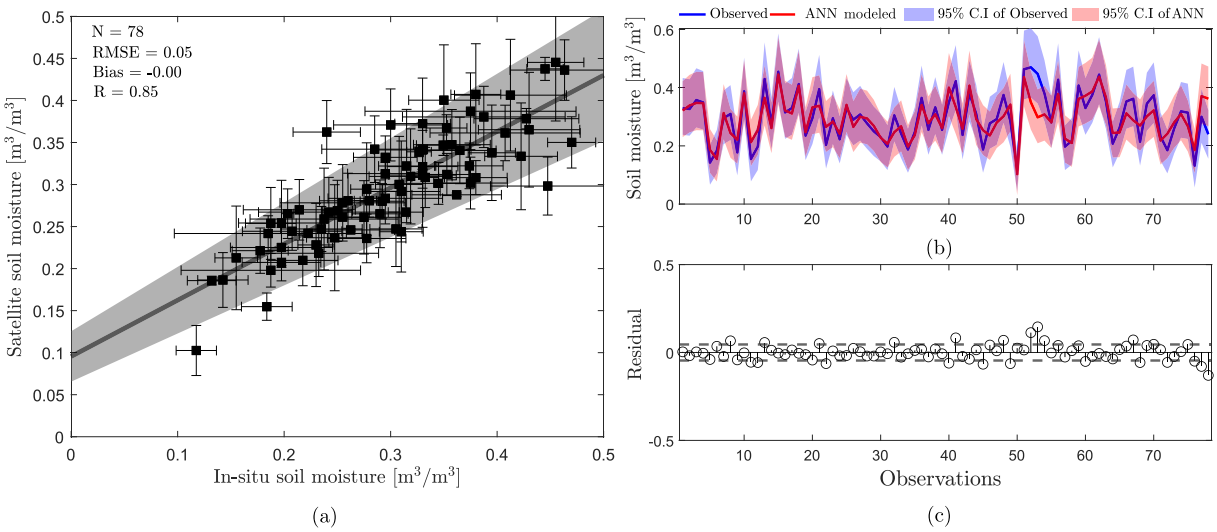


**Fig. 6.** (a) Satellite derived soil moisture (FC-FF-ANN) plotted as a function of in-situ data. Shaded region in gray represents the 95% confidence interval. Horizontal error bar is the standard deviation in the in-situ measurements, the vertical error bar is the model response to the input uncertainties, (b) represents the time series of observed and FC-FF-ANN-derived soil moisture, and (c) represents the corresponding residual plot which is calculated by subtracting fitted values from the in-situ. The dashed lines represent the ±RMSE.

## 3. Materials and methods

### 3.1. Satellite data and processing

We estimate surface soil moisture of the Kosi Fan by using Sentinel-1, Sentinel-2 satellite images, and the digital elevation model from the Shuttle Radar Topography Mission (SRTM) (Table 1). We have downloaded the Sentinel-1 and 2 images from the official website (https://scihub.copernicus.eu/) of the European Space Agency (ESA). The ESA had launched two polar-orbiting satellites, Sentinel-1A (March 2014) and Sentinel-1B (March 2016), under the Copernicus joint initiative of ESA and European Commission (EC). Both these satellite missions share the same orbital plane and carry C-band (5.405 GHz) Synthetic Aperture Radar (SAR).

Sentinel-1A and 1B satellites together acquire images at a temporal resolution of 6-days (12-days individually) into four different modes; wave, extra-wide swath, interferometric wide swath, and stripmap (Singh et al., 2020; DeVries et al., 2020). The images are available in three different levels; level-0, level-1, and level-2. Level-0 is an unfocused SAR product, level-1 is the Ground Range Detected (GRD) and Single Look Complex (SLC), and level-2 is the ocean geophysical product. Single polarisation (*i.e.,* either $\sigma_{VV}$ or $\sigma_{HH}$) is available in the wave mode whereas dual polarisation (*i.e.,* $\sigma_{VV+VH}$ or $\sigma_{HH+HV}$) is available in all other modes. Commonly, $\sigma_{HH}$ or $\sigma_{HH+HV}$ polarisation is available for polar environment and sea-ice zones. The $\sigma_{VV}$ or $\sigma_{VV+VH}$ is accessible for all other regions at a cell size of 10 m × 10 m with 250 km swath. We used $\sigma_{VV+VH}$ dual polarised GRD product (*i.e.,* level-1 product). We performed radiometric correction, multi-looking (with a multi-looking factor of six), speckle filtering through refined Lee filter, and Range-Doppler terrain correction by using Sentinel Application Platform (SNAP v8.0). After the processing, we get the backscatter image at 60 m × 60 m grid size.

Sentinel-2A (launched in June 2015) and Sentinel-2B (launched in March 2017) are two polar-orbiting satellites. The data comes with two levels (1C and 2A) of processing. Level-1C product is top-of-atmosphere, and level-2A is bottom-of-atmosphere corrected (Martins et al., 2017). Sentinel 2A and 2B together acquire images in thirteen different spectral bands (from VNIR to SWIR) at 5 days (10 days individually) revisit time (Li and Roy, 2017). The spatial resolution of these spectral bands varies from 10–60 m. We have selected band 4 (∼ 665 nm) and band 8 (∼ 842 nm) to compute Normalised Difference Vegetation Index (NDVI). The resulting pixel size of the NDVI image is 10 m × 10 m that we have resampled at 60 m × 60 m by using the nearest neighbour algorithm.

We downloaded the SRTM digital elevation model of the study area from the US Geological Survey (https://earthexplorer.usgs.gov). This mission was a joint venture of Agenzia Spaziale Italiana (ASI), NASA, (DoD/NGA) DLR, and National Geospatial-Intelligence Agency that consist of two radars; C-band (by NASA at $\lambda$=5.6 cm) and X-band (by DLR/ASI at $\lambda$=3.1 cm). Three versions of SRTM elevation data are available publicly; SRTM 1 arc-second global, non-void filled, and void filled (Nasa, 2013). We have used void filled DEM elevation data 1 × 1 arc sec (*i.e.,* 30 m × 30 m) that was resampled at 60 m × 60 m.

### 3.2. Measurement

To evaluate the accuracy and reliability of satellite derived soil moisture, we conducted a field campaign during 11$^{th}$ to 20$^{th}$ December 2019 on the Kosi Fan. We have measured surface soil moisture at 78 different locations using a Time Domain Reflectometry (TDR) probe at the time when Sentinel-1 satellite passes over the study area (Fig. 2). Before measuring the soil moisture, we need to calibrate the TDR. This we have done by following the procedures explained in Singh et al. (2020). The penetration depth of Sentinel-1 SAR pulses ranges between 1–5 cm depending upon the target and sensor properties. To ensure that the backscattered SAR pulses sense the same moisture content, we measured the soil moisture at a depth below 5 cm from the ground surface (Singh et al., 2018; Singh et al., 2019). We split the study area into small grids (4 km × 4 km) and then randomly selected a grid using the universal random grid sampling approach. To minimise the impact of spatial heterogeneity at the selected grid, we arbitrarily selected the nearly uniform locations. We then randomly measure soil moisture within a grid at seven to ten different locations by inserting the TDR probe in the top 5 cm of the soil surface. We record the coordinate of each measurement location using a handheld GPS. All our measurements are inside the footprint of the sentinel-1 image pixels (*i.e.,* 60 m), with each observation separated by no less than 20 m apart from the others. To enable a direct point-to-pixel comparison of the in-situ and model-derived soil moisture, we compute the average of these measurements and select the mean value as a single representative of the in-situ measurement (Ryan et al., 2017; Thakur et al., 2018). We used standard deviation to report the uncertainties in our measurements. We have also measured the surface soil roughness in the field by using pin-

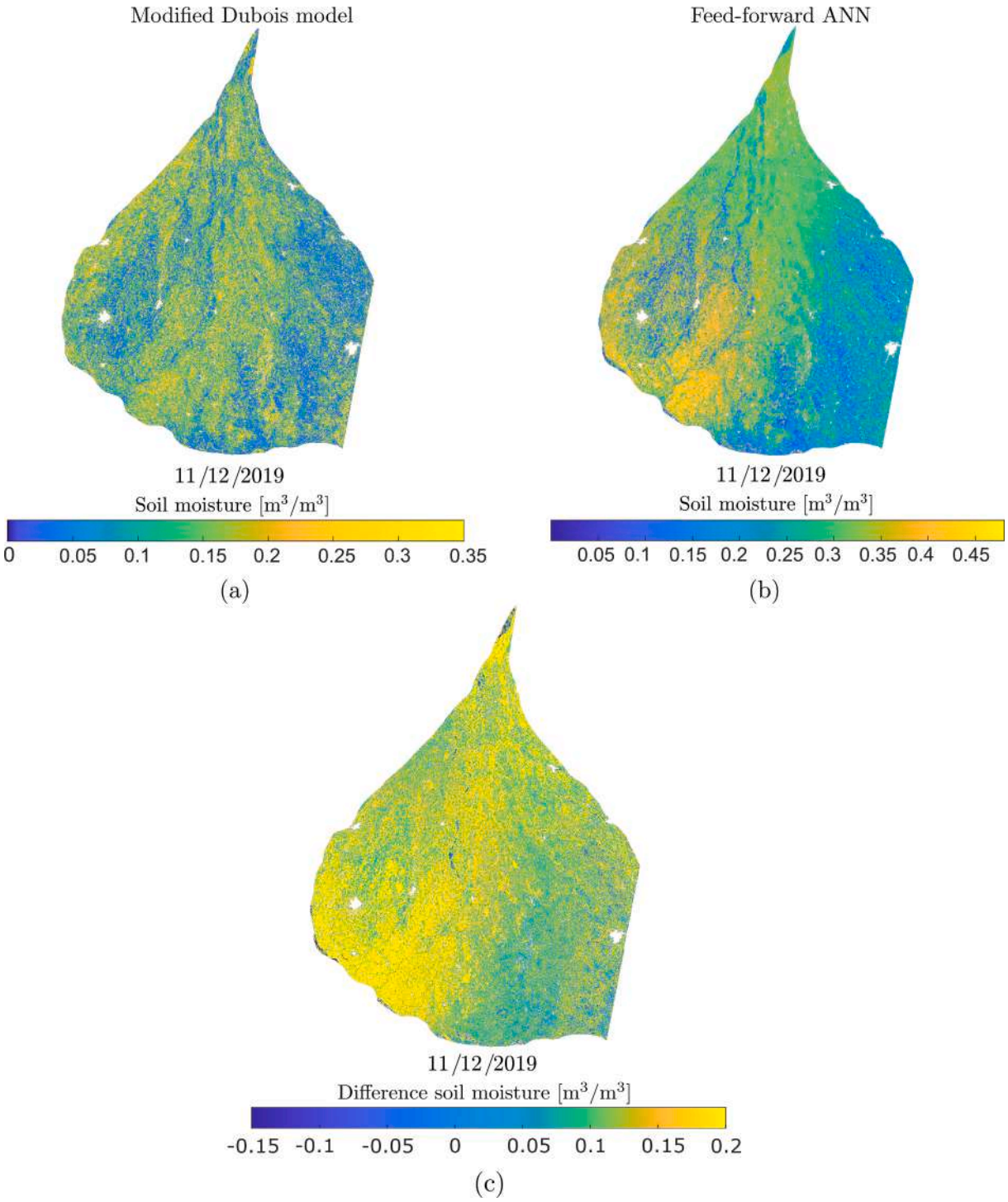


**Fig. 7.** Spatial distribution of the soil moisture (derived from (a) MDM and (b) FC-FF-ANN) on the Kosi Fan. (c) image in the bottom illustrates the difference in soil moisture obtained after subtracting the MDM derived soil moisture from FC-FF-ANN. Transparent pixels are the masked regions.

profilometer (Singh et al., 2021b).

### 3.3. Soil moisture modeling

This section discusses the soil moisture modeling and drainage congestion due to road network. We have written scripts in MATLAB™ for all analysis. The following subsections discuss the detailed procedures to estimate soil moisture using MDM and FC-FF-ANN models.

#### 3.3.1. Modified Dubois model (MDM)

Dubois et al. (1995) proposed an empirical model to estimate soil moisture using quad polarised SAR backscattered images based on X-, C-, and L-band scatterometer and airborne images. They proposed two equations for $\sigma_{HH}$ and $\sigma_{VV}$ (Eqs. 1 and 2) in terms of target parameters ($\epsilon$ and s) and sensor parameters ($\theta$ and $\lambda$). Both the equations are inverted simultaneously to calculate the target parameters.

$$\sigma_{HH} = 10^{-2.75}\left(\frac{\cos^{1.5}\theta}{\sin^{5}\theta}\right)10^{0.028\epsilon\tan\theta}(k{\cdot}s{\cdot}\sin\theta)^{1.4}\lambda^{0.7} \quad (1)$$

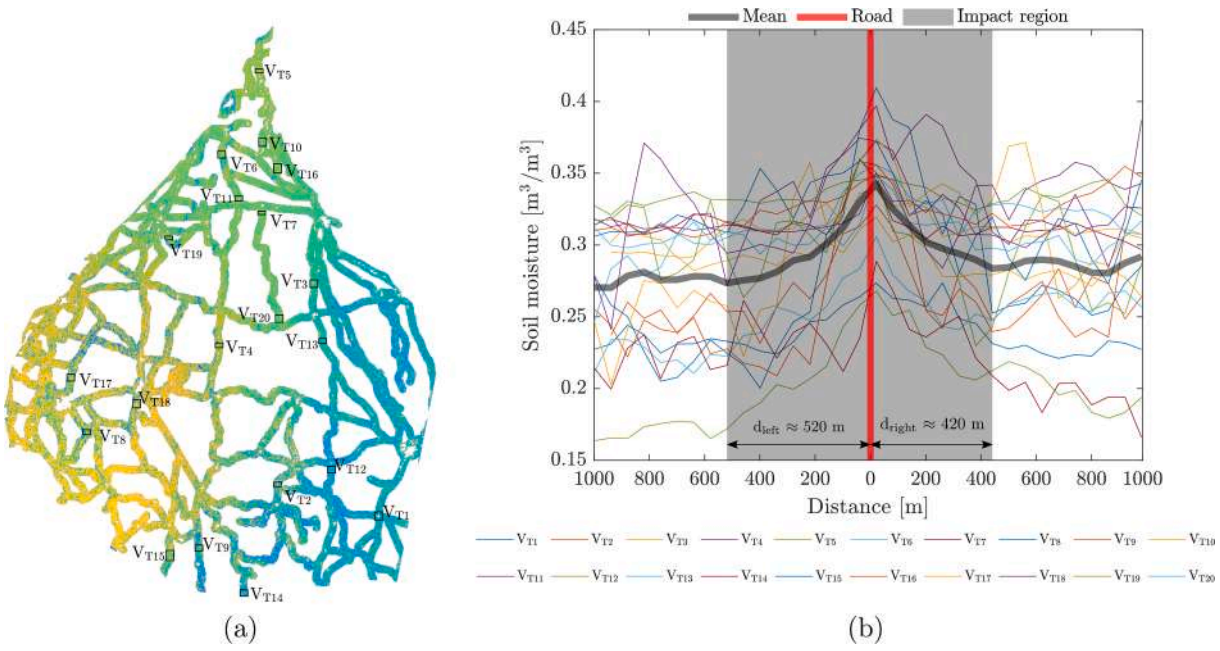


**Fig. 8.** (a) Left panel shows the location of vertical transects on the road soil moisture map with 1 km buffer on either side and (b) right panel shows the soil moisture profile for the corresponding transects. The road is shown in red, and the mean of all the 20 transects is plotted in thick gray.

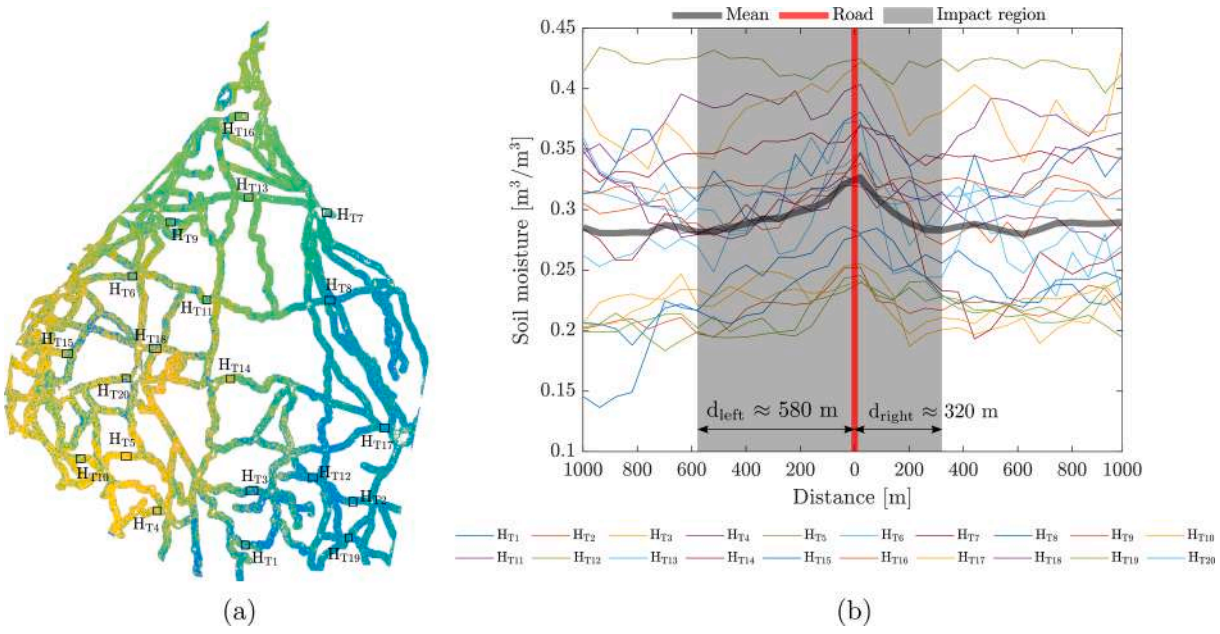


**Fig. 9.** (a) Left panel shows the location of horizontal transects on the road soil moisture map with 1 km buffer on either side, and (b) right panel shows the soil moisture profile for the corresponding transects. The road is shown in red, and the mean of all the 20 transects is plotted in thick gray.

$$\sigma_{VV} = 10^{-2.35}\left(\frac{\cos^3\theta}{\sin^3\theta}\right)10^{0.046\epsilon\tan\theta}(k\cdot s\cdot\sin\theta)^{1.1}\lambda^{0.7} \quad (2)$$

where $\theta$ is the incidence angle, k is the wavenumber ($\frac{2\cdot\pi}{\lambda}$), $\lambda$ is the wavelength of the SAR pulses, $\epsilon$ is the relative soil permittivity, and s is the soil roughness (root mean square height). This model is widely used and can be successfully applied on a sparsely vegetated or barren land where the value of NDVI is less than 0.4 (or region with values $\frac{\sigma_{HV}}{\sigma_{VV}} < -11$ dB) (Dubois et al., 1995). It provides reliable estimates if the soil moisture is within a range between 0–0.35 $m^3/m^3$. Wherever quad polarised SAR images are not available, a modified version of the Dubois model is used (Sahebi and Angles, 2010; Rao et al., 2013; Dave et al., 2019; Singh et al., 2020; Thanabalan et al., 2021). Sahebi and Angles (2010) have eliminated the surface roughness through field measurements and reduced the computation to one equation (either $\sigma_{HH}$ or $\sigma_{VV}$ depending on the availability and satellite mission) with one unknown (*i.e.*, $\epsilon$).

We applied the MDM to estimate the soil permittivity ($\epsilon$) by eliminating the surface roughness through the PCA-MM-SVR model (Singh et al., 2021b). We inverted $\sigma_{VV}$ (Eq. 2) to compute relative soil permittivity and fed it to universal Topp's model to estimate the volumetric surface soil moisture ($m_v$) (Topp et al., 1980).

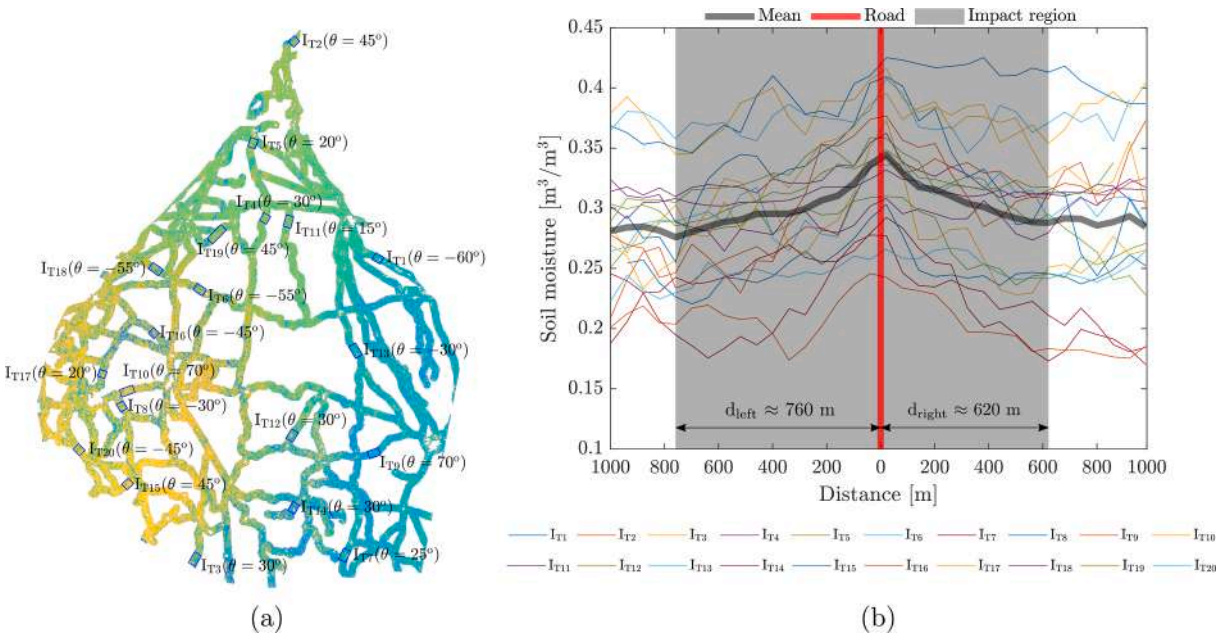


**Fig. 10.** (a) Left panel shows the location of inclined transects on the road soil moisture map with 1 km buffer on either side, and (b) right panel shows the soil moisture profile for the corresponding transects. The road is shown in red, and the mean of all the 20 transects is plotted in thick gray.

### 3.3.2. Feed-forward ANN and data fusion

Machine learning models are widely used to predict soil moisture from satellite images. We trained and applied FC-FF-ANN to obtain the surface soil moisture using the in-situ soil moisture measurements. Initially, we have extracted seven features namely, $\sigma_{HH}, \sigma_{VV}, \theta$, NDVI from Sentinel-1 and Sentinel-2 satellite images respectively, elevation from SRTM-DEM and the coordinate (longitude, and latitude) of each pixel. We generated two extra features (*i.e.,* $\sigma_{VH/VV}$ and $\sigma_{VH-VV}$) via the linear data fusion of $\sigma_{HH}$ and $\sigma_{VV}$ (Singh et al., 2021a). We standardise all the nine features (F) using standard z-score scaling (Eq. 3).

$$F_s = \frac{F - \overline{F}}{\mathrm{std}(F)} \tag{3}$$

where $F_s$ is the standardise, $\overline{F}$ is the mean value (F), and std(F) is the standard deviation of the feature sets. We have randomly divided the feature sets and the corresponding in-situ measurements using the Mersenne Twister generator. We use 40% of the dataset to train a 9:10:10:10:1 (nine inputs, three hidden layers with ten neurons each, and one output) FC-FF-ANN model using Levenberg–Marquardt (LM) training algorithm. We used the remaining datasets to validate (10%) and test (50%) the trained model.

### 3.3.3. Masking built-up regions

We have downloaded the built-up data of the Kosi Fan from Joint Research Centre (JRC) open data portal (https://ghsl.jrc.ec.europa.eu/download.php). This data is a part of the Global Human Settlement Layer (GHSL) that has been derived from Landsat satellite images. The GHS grid contains built-up from 1975 to 2014 in four epoch (*i.e.,* 1975–1990-2000–2014) at different spatial resolution 30 m, 250 m, and 1 km. For this study, we have used the latest available built-up data of 2014 at 250 m spatial resolution. This data product is available in World Mollweide coordinate system. To be consistent with our other data, we have transformed its coordinate to UTM WGS84 and resampled at 60 m grid resolution. Finally, we use this grid to mask the built-up pixels from the soil moisture raster.

## 3.4. Soil moisture in the proximity of road network

We use soil moisture map to study the drainage congestion in the proximity of road network on the Kosi Fan surface. We extract the road network from the Google Earth images. We padded a buffer of 1 km on both sides of the road (Fig. 3a). Within this, we extract the soil moisture along a transect drown across the road network. To check and cover all the possible directional dependency of the road network, we categorised the transects into three major categories; vertical, horizontal, and inclined.

We defined the vertical profiles (*i.e.,* $\alpha = 0^{\circ}$) as a set of transects that travels from up to down (or down to up) parallel to the y-axis (Fig. 3b). An example of a vertical profile is shown in Fig. 3c in blue. We randomly extracted 20 such profiles (*i.e.,* $V_1, V_2, \ldots, V_{20}$) at different locations in the study area. Each profile is an average of 15 to 50 transects. We defined the horizontal profiles as a set of transects from left to right (or right to left) perpendicular to the y-axis (Fig. 3b). In terms of angle, it can be either $\alpha = 90^{\circ}$ or $\alpha = -90^{\circ}$. Fig. 3c (box in red) show a horizontal transect. We have randomly extracted 20 such profiles (*i.e.,* $H_1, H_2, \ldots, H_{20}$) in the study area. Finally, to consider the orientation of a road network other than vertical and horizontal, we have defined inclined profiles. The angles are measured with reference to the y-axis (Fig. 3b). The angles are positive (*i.e.,* $\alpha_+$) in the clockwise and negative (*i.e.,* $\alpha_-$) in the anti-clockwise direction. Fig. 3c (box in green) illustrates the positive angle (*i.e.,* in a clockwise direction). We have randomly extracted 20 such profiles (*i.e.,* $I_1, I_2, \ldots, I_{20}$) at different locations throughout the study area. Fig. 4 illustrates a detailed methodology adopted for this study.

## 4. Results

### 4.1. Modified Dubois model

We plot the soil moisture obtained from MDM against the in-situ observations (Fig. 5a). We noticed MDM is able to capture the trend of spatial variation of soil moisture, however the modelled values are underestimated (with R = 0.43, bias = −0.10, and RMSE = 0.08 $m^3/m^3$). Despite a significant scattering, most of the observation lies within the 95% confidence level. We now plot the time-series of modelled and in-situ soil moisture with the corresponding residuals (Figs. 5b & c). The residuals appears to be stochastic in nature and do not follow any specific pattern. We observed positive residuals in the majority of instances,

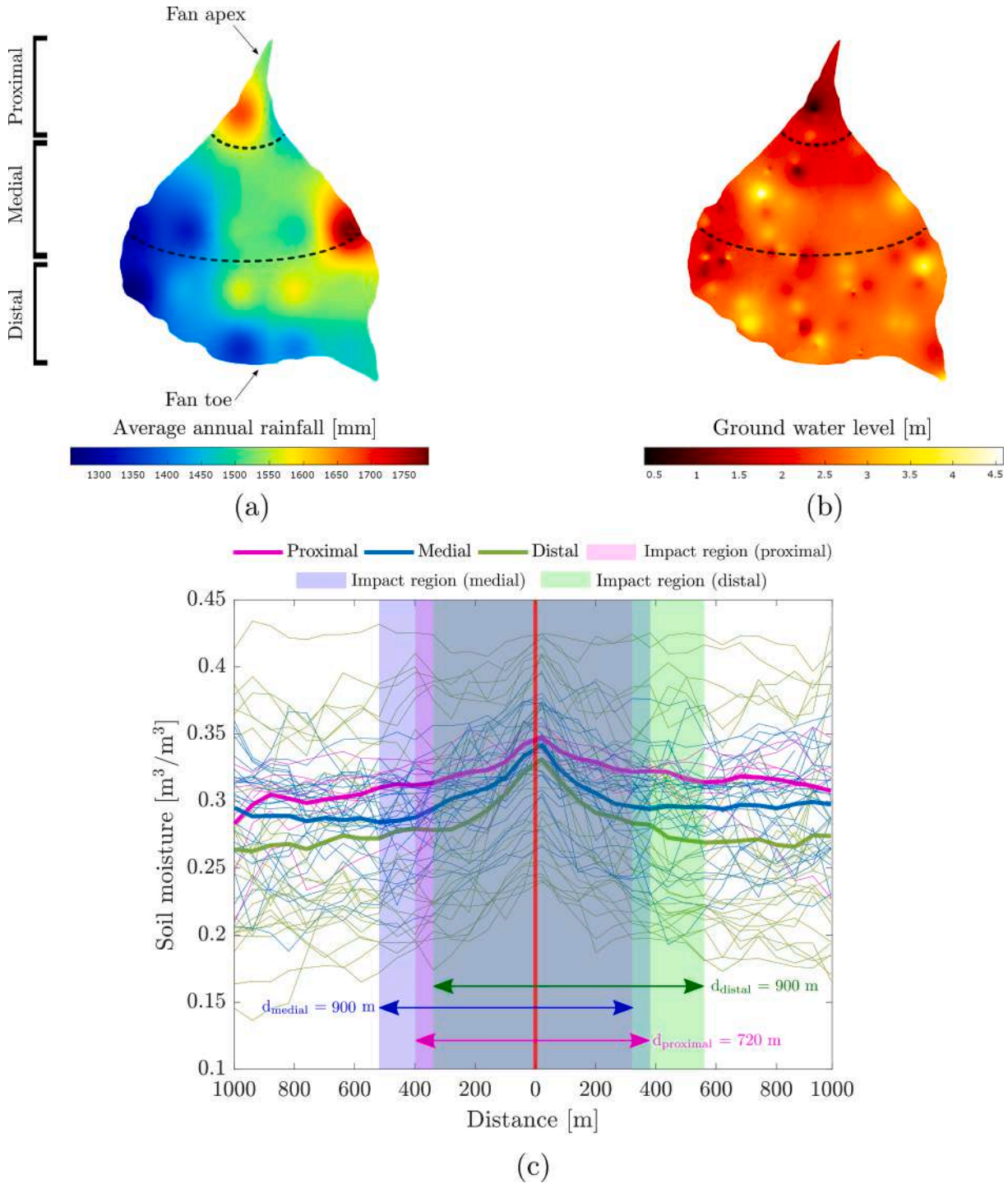


**Fig. 11.** (a) Spatial distribution of average annual rainfall on the Kosi Fan generated using IDW interpolation method for rainfall data from 1980 to 2018 downloaded from India Meteorological Department (IMD) official website (https://mausam.imd.gov.in). (b) spatial distribution of groundwater level (in m b.g.l) using IDW interpolation technique. (c) Variation of the impact region from proximal to the distal part of the Kosi Fan. Vertical line (in red) represents the position of road.

that eventually resulted in a negative bias. Based on these analysis, it is evident that the performance of MDM is reasonably poor on the Kosi Fan.

### 4.2. Feed-forward ANN and data fusion

We now compare the soil moisture predicted from FC-FF-ANN to the in-situ measurement (Fig. 6a). The predicted value accord well with the in-situ measurement (R = 0.85, RMSE = 0.05 $m^3/m^3$, and bias = 0). All the data points are centered along the regression line. Uncertainties of the trained model in response to the input uncertainties are mild. The time-series plot of the predicted soil moisture matches with the in-situ measurements in terms of magnitude and trend (Fig. 6b). The residuals lie within the ± RMSE with no specific pattern. This indicates a good fit (Fig. 6c). Fig. 7 shows the spatial distribution of soil moisture on the Kosi Fan estimated from MDM and FC-FF-ANN. Despite different magnitude, the trend of spatial soil moisture variations appears nearly similar. Table A.1 (Appendix A) reports the comparison of in-situ and

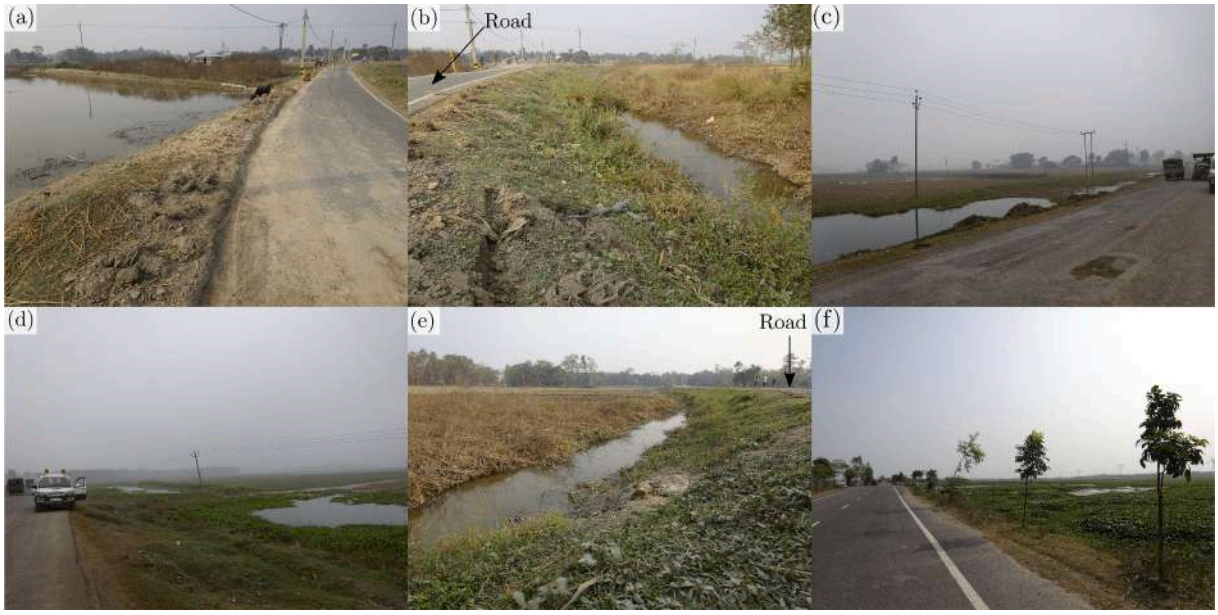


**Fig. 12.** Field photographs (a-f) show the ground condition of drainage congestion and waterlogging at the proximity of road network.

satellite derived soil moisture. It is important to note that the soil moisture derived from MDM is reliable within 0.35 $m^3/m^3$. It does not provide a reliable estimate in the regions where soil moisture contents are relatively high. This is perhaps a reason, MDM is mostly used to estimate soil moisture in the semi-arid/arid regions (Singh et al., 2020). On the Kosi Fan, the surface soil moisture is relatively high due to the presence of numerous active channels and shallow groundwater levels. From here onward, we used the soil moisture estimated from the FC-FF-ANN model.

### 4.3. Drainage congestion due to road network

We extract soil moisture within one km buffer of the road network. We identify the orientation (horizontal, vertical, and inclined) of road network on the Kosi Fan (Fig. 8–10). The rectangular boxes show the location where we extracted the moisture. We plot the soil moisture profile for each vertical transect (Fig. 8a). Interestingly, soil moisture is maximum in the proximity of roads and reduces in the transverse direction as we move farther (Fig. 8b). At some transects we observes the high moisture content at the location farther from the road. This is due to the presence of streams and waterlogging patches that result in high soil moisture. To minimise the impact of these occasional peaks, we have plotted the mean (in black) of all the transects (Fig. 8b). This clearly shows that the road network acts as a barrier due to which soil moisture accumulates along the road resulting into drainage congestion. The region marked in gray shades on either side of the road represents the length up to which effect of the drainage congestion can be clearly observed. Visual observation reveals that the spatial distribution of soil moisture is prominent within the proximity (about 550 m) of the road network, if oriented vertically.

Similarly, we extract soil moisture across the roads oriented horizontally on the Kosi Fan (Fig. 9a). We observed soil moisture content is maximum at the proximity of the road and reduces towards the upward and downward directions from the road. To have a clear trend, we plotted the mean (line in black) of all the transects (Fig. 9b). Visual observation reveals that the spatial distribution of soil moisture is prominent within the proximity (about 600 m) of the road network. Finally, we extract the soil moisture across the roads oriented with some inclination (Fig. 10a). We observed a similar trend as observed for vertical and horizontal profiles. The spatial distribution of soil moisture is prominent within the proximity (about 750 m) of the road network having different orientation angles.

## 5. Discussion

MDM underestimates the surface soil moisture content on the Kosi Fan. This is probably due to the fact that it produces reliable soil moisture (volumetric) estimates within a range between 0–0.35 $m^3/m^3$. Such conditions often prevail in the arid and semi-arid climatic regions. This is why MDM has been widely used to study soil moisture from microwave satellite images in arid/sub-arid regions (Sahebi and Angles, 2010; Rao et al., 2013; Mirsoleimani et al., 2019; Singh et al., 2020). For instance, a very first attempt to estimate surface soil moisture from dual polarised Sentinel-1 SAR image using MDM was executed in the arid region by Sahebi and Angles (2010). They applied MDM on the Chateauguay watershed, Canada. They reported that MDM outperforms the Oh model and Geometrical Optics Model (GOM). Rao et al. (2013) estimated the soil moisture in a semi-arid regions of Vidarbha in Maharashtra. They reported a maximum correlation coefficient of 0.9 with an error of 2.9 %. Recently, a study conducted in the semi-arid region of Karaj (Iran), the authors have used dual polarised Sentinel-1 images to estimate surface soil moisture using MDM (Mirsoleimani et al., 2019). They reported that MDM successfully estimates the surface soil moisture with R = 0.77 and RMSE = 1.45 dB. More recently, Singh et al. (2020) applied the MDM using Sentinel-1 images to calculate the surface soil moisture in a semi-arid region of Central India. They reported that MDM accurately estimate the surface soil moisture over a semi-arid region with R = 0.87, RMSE = 0.035 $m^3/m^3$, and bias = 0.02 $m^3/m^3$. We noticed that the MDM fails to estimate surface soil moisture in the humid climatic regions (*i.e.,* Kosi Fan). The ground measurement suggests a large variability in the surface soil moisture. During our field campaign, we observed the soil moisture varies in a range between 0.10–0.50 $m^3/m^3$, much higher values than the validity range of MDM.

Further, to understand the variation of the drainage congestion with topography, we categorised the Kosi Fan into three regions based on elevation variation; proximal (110–71 m), medial (70–51 m), and distal (50–30 m). We then combined all the 60 transects (*i.e.,* vertical, horizontal, and inclined) and reclassified them based on regions (*i.e.,* proximal, medial, and distal). We plotted transects of the respective regions and estimated the impact region (Fig. 11c). We noticed in the proximal part, the total impact region is approximately 700 m. For the medial and distal portions, we observed nearly the same impact region of 900 m.

Interestingly, we found that the drainage congestion intensity (in terms of soil moisture) is highest in the proximal part, followed by the medial and distal part, respectively. The highest intensity in the proximal region is in accordance with the shallow groundwater level. Next, as compared to the distal region, the groundwater level is relatively deeper in the medial part. This is in accordance with the drainage congestion, which ranked second in terms of intensity. Lastly, we observed a similar trend in the distal region, which ranked last in terms of drainage congestion. However, considering the elevation solely may result in biased observations. For a fair linkage, we created the spatial maps of the annual rainfall and groundwater level (Figs. 11a & b). We found that the average annual rainfall in the proximal part of the Fan ranges between 1450 to 1700 mm; in the medial region, it varies between 1300 to 1750 mm, and in the distal part, it ranges between 1250 to 1700 mm. In comparison, the groundwater level in the proximal portion ranges between 0.5 to 1.5 m; in the medial and distal part, it ranges between 1 to 4.5 m.

As discussed, regions of drainage congestion due to structural barriers (*i.e.,* road, embankment) may convert into permanent waterlogging, if sustained for a longer period. We can observe a severe waterlogged condition along both sides of the road (Fig. 12). Such a situation may trigger permanent damage, deformation, or collapse of the road network. Most importantly, the majority of the roads on the Kosi Fan passes through the agricultural lands, which directly affects the farm yield. The accumulation of water can result in poor soil aeration, that can eventually degrade the overall productivity of the soil (Prajapati et al., 2021). These conditions can be minimised by maintaining the natural drainage by providing proper passages for water to move downstream at the time of planning and execution of road construction (Khalil et al., 2021). This will avoid accumulation of water due to drainage blockage.

## 6. Conclusion

This study uses soil moisture as a proxy to assess drainage congestion in the proximity of road network on the alluvial fan of the Kosi river in the Himalayan Foreland. We used remote sensing (microwave and optical) images and ground measurements to estimate surface soil moisture by using a semi-empirical (MDM) and data driven machine learning (FC-FF-ANN) models. Based on this study following conclusions can be drawn;

- On the Kosi Fan, FC-FF-ANN model predicts the soil moisture more accurately than MDM.
- Road network acts as a physical barrier and leads to drainage congestion at several places. This eventually results in high soil moisture in the proximity of the road network.
- The extent of drainage congestion is different for the road network oriented in vertical, horizontal, and inclined direction. The extent of drainage congestion is relatively more at the locations where roads traverse in inclined direction.
- The impact of drainage congestion along the road network is more prominent in the medial, and distal parts than the proximal region of the Kosi Fan.
- Soil moisture information can be used as a precursor to measure the drainage congestion along the road network.

This comprehensive framework is a first step to monitor the drainage congestion along the road network from remote sensing images. Publicly available satellite images (*i.e.,* Landsat, Sentinel-2, Sentinel-1) provide images of the earth's surface at high spatial and temporal resolution. They can be used to monitor the drainage congestion and soil moisture variability in near real time. Such measurements would help policy-makers to make much informed decisions in the planning and execution of development works in the flood prone regions.

The outcome of this study will help to prevent or mitigate the losses due to the severe drainage congestion in terms of agricultural yield, public health, soil health, and flood hazards on the alluvial fans.

## Authors contributions

Field work (A.S), Model development and software (A.S and K.G), Procedure (A.S, M.N.N, and K.G), Investigation (A.S and K.G), Resources (K.G), Writing - First draft (A.S and K.G), Writing - Review Editing (A.S and K.G), Visualization (A.S, M.N.N, and K.G), Supervision and funding (K.G).

## Funding

The Science and Engineering Research Board (SERB) of India provided funding for this study under grant ECR/2017/001154.

## Data availability

The MATLAB scripts developed in this study can be made available on a resonable request to the corresponding author. The in-situ soil moisture data is provided in Table A.1.

## Declaration of Competing Interest

The authors declare that they have no known competing financial interests or personal relationships that could have appeared to influence the work reported in this paper.

## Acknowledgments

We acknowledge IISER Bhopal for providing institutional support. AS would like to acknowledge the Department of Science and Technology (DST), Government of India for providing funding to pursue PhD through the DST-INSPIRE fellowship (grant no. DST/INSPIRE Fellowship/IF180001) scheme. We acknowledge the Science and Engineering Research Board (SERB), Govt. of India for providing financial support through grant ECR/2017/001154. We are thankful to the editor and all the anonymous reviewers for their constructive comments and suggestions.

## Appendix A. Soil moisture measurements

This appendix consist of Table A.1.

**Table A.1**
Comparison of in-situ soil moisture with satellite derived soil moisture.

| Site ID | Longitude | Latitude | In-situ | Satellite | |
|---|---|---|---|---|---|
| | | | | MDM | FC-FF-ANN |
| 1 | 86.63923 | 26.13257 | 0.375 | 0.116 | 0.387 |
| 2 | 86.64361 | 26.10979 | 0.330 | 0.207 | 0.321 |
| 3 | 86.62364 | 26.09691 | 0.350 | 0.203 | 0.400 |
| 4 | 86.62604 | 26.0954 | 0.327 | 0.175 | 0.339 |
| 5 | 86.62061 | 26.0632 | 0.358 | 0.102 | 0.347 |
| 6 | 86.566 | 26.0243 | 0.285 | 0.112 | 0.342 |
| 7 | 86.57533 | 25.97547 | 0.349 | 0.083 | 0.347 |
| 8 | 86.64431 | 25.99772 | 0.118 | 0.052 | 0.103 |
| 9 | 86.64072 | 26.03379 | 0.143 | 0.045 | 0.186 |
| 10 | 86.62675 | 26.15357 | 0.463 | 0.309 | 0.436 |
| 11 | 86.66584 | 26.19629 | 0.470 | 0.227 | 0.350 |
| 12 | 86.6998 | 26.21087 | 0.448 | 0.155 | 0.298 |
| 13 | 86.73994 | 26.22444 | 0.380 | 0.209 | 0.407 |
| 14 | 86.75186 | 26.23693 | 0.184 | 0.059 | 0.155 |
| 15 | 86.78488 | 26.24503 | 0.295 | 0.192 | 0.313 |
| 16 | 86.79723 | 26.26185 | 0.423 | 0.249 | 0.334 |
| 17 | 86.80273 | 26.2389 | 0.280 | 0.197 | 0.281 |

(*continued on next page*)

**Table A.1** (*continued*)

| Site ID | Longitude | Latitude | In-situ | Satellite | |
|---|---|---|---|---|---|
| | | | | MDM | FC-FF-ANN |
| 18 | 86.79795 | 26.20753 | 0.428 | 0.309 | 0.378 |
| 19 | 86.79031 | 26.18241 | 0.310 | 0.081 | 0.244 |
| 20 | 86.76803 | 26.1514 | 0.178 | 0.011 | 0.221 |
| 21 | 86.65507 | 26.11443 | 0.388 | 0.213 | 0.380 |
| 22 | 86.70612 | 26.06255 | 0.155 | 0.118 | 0.213 |
| 23 | 86.73248 | 26.04625 | 0.238 | 0.039 | 0.259 |
| 24 | 86.71229 | 26.03606 | 0.198 | 0.046 | 0.254 |
| 25 | 86.75741 | 26.02952 | 0.430 | 0.127 | 0.365 |
| 26 | 86.75144 | 25.91161 | 0.275 | 0.079 | 0.261 |
| 27 | 86.66203 | 25.86703 | 0.198 | 0.075 | 0.207 |
| 28 | 86.68053 | 25.82926 | 0.218 | 0.268 | 0.210 |
| 29 | 86.68639 | 25.78836 | 0.380 | 0.318 | 0.308 |
| 30 | 86.6876 | 25.74611 | 0.408 | 0.385 | 0.361 |
| 31 | 86.71125 | 25.6878 | 0.455 | 0.348 | 0.445 |
| 32 | 86.69384 | 25.70237 | 0.330 | 0.340 | 0.311 |
| 33 | 86.65567 | 25.72331 | 0.375 | 0.175 | 0.302 |
| 34 | 86.6099 | 25.72783 | 0.445 | 0.241 | 0.438 |
| 35 | 86.57812 | 25.7314 | 0.315 | 0.275 | 0.322 |
| 36 | 86.54615 | 25.77154 | 0.353 | 0.361 | 0.367 |
| 37 | 86.52457 | 25.80515 | 0.330 | 0.186 | 0.341 |
| 38 | 86.53774 | 25.85775 | 0.413 | 0.294 | 0.406 |
| 39 | 86.56369 | 25.8713 | 0.235 | 0.084 | 0.247 |
| 40 | 86.80625 | 25.91648 | 0.208 | 0.254 | 0.244 |
| 41 | 86.93388 | 25.89581 | 0.295 | 0.268 | 0.332 |
| 42 | 87.00225 | 25.90533 | 0.395 | 0.243 | 0.338 |
| 43 | 87.06107 | 25.90827 | 0.203 | 0.220 | 0.265 |
| 44 | 87.09836 | 25.92137 | 0.310 | 0.225 | 0.292 |
| 45 | 87.21534 | 25.88781 | 0.295 | 0.314 | 0.284 |
| 46 | 87.46254 | 25.72741 | 0.263 | 0.220 | 0.246 |
| 47 | 87.42014 | 25.6838 | 0.223 | 0.196 | 0.242 |
| 48 | 87.39914 | 25.64069 | 0.330 | 0.348 | 0.372 |
| 49 | 87.39871 | 25.60628 | 0.290 | 0.243 | 0.265 |
| 50 | 87.42513 | 25.61369 | 0.188 | 0.270 | 0.254 |
| 51 | 87.475 | 25.60035 | 0.308 | 0.272 | 0.300 |
| 52 | 87.48171 | 25.59672 | 0.353 | 0.315 | 0.312 |
| 53 | 87.55177 | 25.60905 | 0.278 | 0.305 | 0.294 |
| 54 | 87.54285 | 25.62759 | 0.250 | 0.244 | 0.269 |
| 55 | 87.53111 | 25.65317 | 0.230 | 0.252 | 0.228 |
| 56 | 87.52139 | 25.67509 | 0.198 | 0.132 | 0.225 |
| 57 | 87.51138 | 25.70004 | 0.305 | 0.245 | 0.247 |
| 58 | 87.51614 | 25.81319 | 0.278 | 0.165 | 0.236 |
| 59 | 87.52789 | 25.82046 | 0.362 | 0.184 | 0.288 |
| 60 | 87.54014 | 25.91021 | 0.214 | 0.283 | 0.270 |
| 61 | 87.51805 | 25.99278 | 0.242 | 0.143 | 0.267 |
| 62 | 87.50936 | 26.00962 | 0.188 | 0.054 | 0.198 |
| 63 | 87.46062 | 26.12101 | 0.345 | 0.210 | 0.301 |
| 64 | 87.29737 | 26.22082 | 0.374 | 0.193 | 0.322 |
| 65 | 87.27813 | 26.24172 | 0.233 | 0.171 | 0.218 |
| 66 | 87.23487 | 26.27511 | 0.248 | 0.282 | 0.237 |
| 67 | 87.2269 | 26.24339 | 0.185 | 0.158 | 0.242 |
| 68 | 87.2321 | 26.20331 | 0.365 | 0.192 | 0.341 |
| 69 | 87.23437 | 26.17834 | 0.255 | 0.124 | 0.278 |
| 70 | 87.23401 | 26.13083 | 0.260 | 0.244 | 0.281 |
| 71 | 87.25929 | 26.01328 | 0.333 | 0.158 | 0.308 |
| 72 | 87.30746 | 25.93218 | 0.255 | 0.208 | 0.261 |
| 73 | 87.20622 | 26.326 | 0.319 | 0.274 | 0.310 |
| 74 | 87.034 | 26.29657 | 0.314 | 0.149 | 0.267 |
| 75 | 87.00787 | 26.17258 | 0.292 | 0.122 | 0.280 |
| 76 | 86.99307 | 26.05495 | 0.132 | 0.178 | 0.186 |
| 77 | 86.97813 | 25.77722 | 0.300 | 0.318 | 0.371 |
| 78 | 86.96597 | 25.71033 | 0.240 | 0.283 | 0.362 |

## References


Abowarda, A.S., Bai, L., Zhang, C., Long, D., Li, X., Huang, Q., Sun, Z., 2021. Generating surface soil moisture at 30 m spatial resolution using both data fusion and machine learning toward better water resources management at the field scale. Remote Sens. Environ. 255, 112301.

den Besten, N., Steele-Dunne, S., de Jeu, R., van der Zaag, P., 2021. Towards monitoring waterlogging with remote sensing for sustainable irrigated agriculture. Remote Sens. 13, 2929.

Chandio, A., Lee, T., Mirjat, M., 2012. The extent of waterlogging in the lower indus basin (pakistan)–a modeling study of groundwater levels. J. Hydrol. 426, 103–111.

Ciancio, N., Miralles, D.J., Striker, G.G., Abeledo, L.G., 2021. Plant growth rate after, and not during, waterlogging better correlates to yield responses in wheat and barley. J. Agron. Crop Sci. 207, 304–316.

Crow, W.T., Chen, F., Reichle, R.H., Liu, Q., 2017. L band microwave remote sensing and land data assimilation improve the representation of prestorm soil moisture conditions for hydrologic forecasting. Geophys. Res. Lett. 44, 5495–5503.

Dave, R., Kumar, G., Kr. Pandey, D., Khan, A., Bhattacharya, B., 2019. Evaluation of modified dubois model for estimating surface soil moisture using dual polarization risat-1 c-band sar data. Geocarto Int. 1–11.

DeVries, B., Huang, C., Armston, J., Huang, W., Jones, J.W., Lang, M.W., 2020. Rapid and robust monitoring of flood events using sentinel-1 and landsat data on the google earth engine. Remote Sens. Environ. 240, 111664.

Dubois, P.C., Van Zyl, J., Engman, T., 1995. Measuring soil moisture with imaging radars. IEEE Trans. Geosci. Remote Sens. 33, 915–926.

Florinsky, I., 2016. Digital terrain analysis in soil science and geology. Academic Press.

Gaurav, K., Métivier, F., Devauchelle, O., Sinha, R., Chauvet, H., Houssais, M., Bouquerel, H., 2015. Morphology of the kosi megafan channels. Earth Surface Dynam. 3, 321–331.

Gaurav, K., Tandon, S., Devauchelle, O., Sinha, R., Métivier, F., 2017. A single width–discharge regime relationship for individual threads of braided and meandering rivers from the himalayan foreland. Geomorphology 295, 126–133.

Hatton, T., Bartle, G., Silberstein, R., Salama, R., Hodgson, G., Ward, P., Lambert, P., Williamson, D., 2002. Predicting and controlling water logging and groundwater flow in sloping duplex soils in western australia. Agric. Water Manag. 53, 57–81.

Jalayer, F., De Risi, R., De Paola, F., Giugni, M., Manfredi, G., Gasparini, P., Topa, M.E., Yonas, N., Yeshitela, K., Nebebe, A., et al., 2014. Probabilistic gis-based method for delineation of urban flooding risk hotspots. Nat. Hazards 73, 975–1001.

Kaushik, S., Dhote, P.R., Thakur, P.K., Nikam, B.R., Aggarwal, S.P., 2019. An integrated approach for identification of waterlogged areas using rs and gis technique and groundwater modelling. Sustain. Water Resources Manage. 5, 1887–1901.

Khalil, M.M., Abotalib, A.Z., Farag, M.H., Rabei, M., Abdelhady, A.A., Pichler, T., 2021. Poor drainage-induced waterlogging in saharan groundwater-irrigated lands: Integration of geospatial, geophysical, and hydrogeological techniques. Catena 207, 105615.

Kumar, R., Jain, V., Babu, G.P., Sinha, R., 2014. Connectivity structure of the kosi megafan and role of rail-road transport network. Geomorphology 227, 73–86.

Li, J., Roy, D.P., 2017. A global analysis of sentinel-2a, sentinel-2b and landsat-8 data revisit intervals and implications for terrestrial monitoring. Remote Sensing 9, 902.

Martins, V.S., Barbosa, C.C.F., De Carvalho, L.A.S., Jorge, D.S.F., Lobo, F.d.L., Novo, E.M. L.d.M., 2017. Assessment of atmospheric correction methods for sentinel-2 msi images applied to amazon floodplain lakes. Remote Sensing 9, 322.

McFarlane, D., 1985. Assessment of waterlogged sites. Journal of the Department of Agriculture, Western Australia, Series 4 26, 119–121.

Mirsoleimani, H.R., Sahebi, M.R., Baghdadi, N., El Hajj, M., 2019. Bare soil surface moisture retrieval from sentinel-1 sar data based on the calibrated iem and dubois models using neural networks. Sensors 19, 3209.

Mishra, K., Sinha, R., 2020. Flood risk assessment in the kosi megafan using multi-criteria decision analysis: A hydro-geomorphic approach. Geomorphology 350, 106861.

Nasa, J., 2013. Nasa shuttle radar topography mission global 1 arc second. Nasa Lp Daac 15.

NRSC, 2017; accessed on 25 March 2021). District and category wise distribution of Land Use and Land Cover in Bihar (2015–16). URL: https://bhuvan-app1.nrsc.gov.in/2dresources/thematic/LULC503/MAP/BR.pdf.

Pandey, A., Singh, S.K., Nathawat, M., 2012. Analysing the impact of anthropogenic activities on waterlogging dynamics in indo-gangetic plains, northern bihar, india. Int. J. Remote Sens. 33, 135–149.

Prajapati, G.S., Rai, P.K., Mishra, V.N., Singh, P., Shahi, A.P., 2021. Remote sensing-based assessment of waterlogging and soil salinity: a case study from kerala, india. Results Geophys. Sci. 7, 100024.

Rao, S.S., Das, S., Nagaraju, M., Venugopal, M., Rajankar, P., Laghate, P., Reddy, M.S., Joshi, A., Sharma, J., et al., 2013. Modified dubois model for estimating soil moisture with dual polarized sar data. J. Indian Soc. Remote Sens. 41, 865–872.

Ryan, J., Hubbard, A., Irvine-Fynn, T.D., Doyle, S.H., Cook, J., Stibal, M., Box, J., 2017. How robust are in situ observations for validating satellite-derived albedo over the dark zone of the greenland ice sheet? Geophys. Res. Lett. 44, 6218–6225.

Sahebi, M., Angles, J., 2010. An inversion method based on multi-angular approaches for estimating bare soil surface parameters from radarsat-1. Hydrol. Earth Syst. Sci. 14, 2355–2366.

Seibert, J., Stendahl, J., Sørensen, R., 2007. Topographical influences on soil properties in boreal forests. Geoderma 141, 139–148.

Singh, A., Gaurav, K., Beg, Z., Rai, A.K., 2021a. Machine learning and data fusion to estimate soil moisture from remote sensing data, in: AGU Fall Meeting 2021, AGU.

Singh, A., Gaurav, K., Meena, G.K., Kumar, S., 2020. Estimation of soil moisture applying modified dubois model to sentinel-1; a regional study from central india. Remote Sensing 12, 2266.

Singh, A., Gaurav, K., Rai, A.K., Beg, Z., 2021b. Machine learning to estimate surface roughness from satellite images. Remote Sensing 13, 3794.

Singh, A., Meena, G.K., Kumar, S., Gaurav, K., 2018. Analysis of the effect of incidence angle and moisture content on the penetration depth of l-and s-band sar signals into the ground surface. ISPRS Annals of Photogrammetry, Remote Sensing & Spatial Information Sciences 4.

Singh, A., Meena, G.K., Kumar, S., Gaurav, K., 2019. Evaluation of the penetration depth of l-and s-band (nisar mission) microwave sar signals into ground. In: 2019 URSI Asia-Pacific Radio Science Conference (AP-RASC), IEEE, pp. 1–1.

Singh, M., Sinha, R., 2022. A basin-scale inventory and hydrodynamics of floodplain wetlands based on time-series of remote sensing data. Remote Sens. Lett. 13, 1–13. https://doi.org/10.1080/2150704X.2021.1980919.
Sinha, R., 2009. The great avulsion of kosi on 18 august 2008. Curr. Sci. 429–433.
Sinha, R., 2014. The kosi megafan: the best-known himalayan megafan. Landscapes and landforms of India. Springer 151–156.
Sinha, R., Bapalu, G., Singh, L., Rath, B., 2008. Flood risk analysis in the kosi river basin, North Bihar using multi-parametric approach of analytical hierarchy process (ahp). J. Indian Soc. Remote Sens. 36, 335–349.
Sinha, R., Gaurav, K., Chandra, S., Tandon, S., 2013. Exploring the channel connectivity structure of the august 2008 avulsion belt of the kosi river, india: Application to flood risk assessment. Geology 41, 1099–1102.
Sinha, R., Gupta, S., Nepal, S., 2018. Groundwater dynamics in north bihar plains. Curr. Sci. 114, 2482–2493.
Steffens, D., Hutsch, B., Eschholz, T., Losak, T., Schubert, S., 2005. Water logging may inhibit plant growth primarily by nutrient deficiency rather than nutrient toxicity. Plant Soil Environ. 51, 545.
Thakur, K.K., Vanderstichel, R., Barrell, J., Stryhn, H., Patanasatienkul, T., Revie, C.W., 2018. Comparison of remotely-sensed sea surface temperature and salinity products with in situ measurements from british columbia, canada. Front. Mar. Sci. 5, 121.
Thanabalan, P., Vidhya, R., Kankara, R., 2021. Soil moisture estimation using risat-1 and sentinel-1 data using modified dubois modelin comparison with averaged ndvi. Geocarto Int. 1–15.
Topp, G.C., Davis, J., Annan, A.P., 1980. Electromagnetic determination of soil water content: Measurements in coaxial transmission lines. Water Resour. Res. 16, 574–582.
Wells, N.A., Dorr Jr, J.A., 1987. Shifting of the kosi river, northern india. Geology 15, 204–207.
Yuan, Y., Liu, S., Wu, M., Zhong, M., Shahid, M.Z., Liu, Y., 2021. Effects of topography and soil properties on the distribution and fractionation of rees in topsoil: A case study in sichuan basin, china. Sci. Total Environ. 791, 148404.